

High-Resolution Satellite Measurements of the Atmospheric Boundary Layer Response to SST Variations along the Agulhas Return Current

LARRY W. O'NEILL, DUDLEY B. CHELTON, AND STEVEN K. ESBENSEN

College of Oceanic and Atmospheric Sciences, Oregon State University, Corvallis, Oregon

FRANK J. WENTZ

Remote Sensing Systems, Santa Rosa, California

(Manuscript received 11 March 2004, in final form 30 September 2004)

ABSTRACT

The marine atmospheric boundary layer (MABL) response to sea surface temperature (SST) perturbations with wavelengths shorter than 30° longitude by 10° latitude along the Agulhas Return Current (ARC) is described from the first year of SST and cloud liquid water (CLW) measurements from the Advanced Microwave Scanning Radiometer (AMSR) on the Earth Observing System (EOS) *Aqua* satellite and surface wind stress measurements from the QuikSCAT scatterometer. AMSR measurements of SST at a resolution of 58 km considerably improves upon a previous analysis that used the Reynolds SST analyses, which underestimate the short-scale SST gradient magnitude over the ARC region by more than a factor of 5. The AMSR SST data thus provide the first quantitatively accurate depiction of the SST-induced MABL response along the ARC. Warm (cold) SST perturbations produce positive (negative) wind stress magnitude perturbations, leading to short-scale perturbations in the wind stress curl and divergence fields that are linearly related to the crosswind and downwind components of the SST gradient, respectively. The magnitudes of the curl and divergence responses vary seasonally and spatially with a response nearly twice as strong during the winter than during the summer along a zonal band between 40° and 50° S. These seasonal variations closely correspond to seasonal and spatial variability of large-scale MABL stability and surface sensible heat flux estimated from NCEP reanalysis fields. SST-induced deepening of the MABL over warm water is evident in AMSR measurements of CLW. Typical annual mean differences in cloud thickness between cold and warm SST perturbations are estimated to be about 300 m.

1. Introduction

The Agulhas Return Current (ARC) separates warm subtropical water to the north from cold subpolar water to the south and marks the location of vigorous air-sea interaction processes (e.g., Jury and Walker 1988; Jury 1994; Rouault and Lutjeharms 2000; O'Neill et al. 2003, hereafter referred to as OCE). Large, quasi-stationary meanders in the sea surface temperature (SST) front associated with the ARC coincide with the location of the Agulhas Plateau and the Mozambique Escarpment (Lutjeharms and van Ballegooyen 1984). As the winds blow across these meanders, the sharp SST front mod-

ifies the marine atmospheric boundary layer (MABL), resulting in perturbations in surface winds and cloud cover. Annually averaged SST gradients across the ARC exceed $4^\circ\text{C} (100 \text{ km})^{-1}$ in some regions, which are among the strongest in the World Ocean. All-weather satellite SST measurements with a resolution of about 58 km have recently become available for the first time over the ARC from the Advanced Microwave Scanning Radiometer (AMSR) on the Earth Observing System (EOS) *Aqua* satellite. The objective of this study is to quantify the influence of SST on surface winds and clouds using the first 12 months of SST and cloud liquid water (CLW) measurements from the AMSR and coincident wind stress measurements from the QuikSCAT scatterometer.

The mechanisms governing the SST influence on surface winds have been identified in various areas of the World Ocean from in situ observations (e.g., Sweet et

Corresponding author address: Larry W. O'Neill, College of Oceanic and Atmospheric Sciences, Oregon State University, 104 COAS Admin. Bldg., Corvallis, OR, 97331-5503.
E-mail: loneill@coas.oregonstate.edu

al. 1981; Hsu 1984a; Jury and Walker 1988; Rogers 1989; Hayes et al. 1989; Wallace et al. 1989; Freije et al. 1991; Bond 1992; Jury 1994; Kwon et al. 1998; Rouault and Lutjeharms 2000; Hashizume et al. 2002; Thum et al. 2002; Cronin et al. 2003), analytical models (Hsu 1984b; Lindzen and Nigam 1987), and mesoscale atmospheric models (e.g., Wai and Stage 1989; Warner et al. 1990; Koraćin and Rogers 1990; Xie et al. 1998; de Szoeke and Bretherton 2004; Small et al. 2003, 2005). SST gradients influence the MABL by modifying its stability through changes in air–sea heat flux and through the development of secondary circulations. Over colder water, decreased surface heat fluxes stabilize the MABL, inhibiting the vertical turbulent mixing of momentum from aloft to the surface, increasing the near-surface wind shear, and decelerating the surface winds. Over warmer water, increased surface heat fluxes destabilize and deepen the MABL, enhancing the vertical turbulent mixing of momentum from aloft to the surface, while reducing the near-surface wind shear, and accelerating the surface winds. Previous studies by Chelton et al. (2001), OCE, and Chelton et al. (2004) have shown that the decelerations and accelerations of surface winds lead to convergences and divergences in the surface wind field that are linearly related to the downwind component of the SST gradient; likewise, crosswind gradients in the SST field generate lateral variations in MABL stability, resulting in a curl of the surface wind field. A hydrostatic pressure gradient also develops across SST fronts with higher pressure and descending air over the colder water and lower pressure and ascending air over the warmer water, forming thermally direct circulations in the MABL over the SST front that enhance the cross-frontal surface flow from colder to warmer water.

MABL clouds form preferentially over the warm, downwind side of SST fronts (e.g., Wai and Stage 1989; Rogers 1989; Deser et al. 1993; Hashizume et al. 2001; Xie et al. 2001). Over the ARC and the Agulhas Current, increases in surface fluxes and decreases in MABL stability are associated with the increased formation of stratocumulus clouds over the warmest SSTs compared to adjacent colder water (Lutjeharms et al. 1986; Lee-Thorp et al. 1998). Large surface heat fluxes over the ARC and the Agulhas Current have been observed to accompany decreases in MABL stability as the large-scale winds blow from cold to warm water (e.g., Rouault and Lee-Thorp 1996; Lee-Thorp et al. 1999; Rouault and Lutjeharms 2000). These studies suggest that stability-dependent turbulent mixing regulates MABL cloud formation by deepening the MABL and by controlling the vertical mixing of moisture and heat

from the surface upward past the lifting condensation level.

Satellite measurements of surface winds, SST, surface heat fluxes, and clouds have shown that the mesoscale coupling between SST fronts and the MABL observed in regional, in situ studies occurs worldwide wherever large SST gradients exist. The eastern tropical Pacific has received the most attention (e.g., Deser et al. 1993; Xie et al. 1998; Liu et al. 2000; Chelton et al. 2001; Hashizume et al. 2001; Thum et al. 2002). Recent studies have focused on the North Pacific (Nonaka and Xie 2003; Chelton et al. 2004), the North Atlantic (Chelton et al. 2004), and the Southern Ocean (OCE; White and Annis 2003). These observations are consistent with the conclusions reached from in situ observations that SST fronts alter MABL stability, thereby influencing the surface winds and the development of low-level clouds.

The accuracy of SST measurements used in air–sea interaction studies over the Southern Ocean is an important issue (e.g., OCE). At these high southern latitudes, in situ observations of SST are very sparse. Furthermore, clouds that cover more than 75% of the Southern Ocean surface in the annual mean (e.g., Rossow and Schiffer 1991; Hahn et al. 1995) introduce biases and errors in infrared measurements of SST due to errors in cloud detection algorithms. To mitigate the effects of these biases and uncertainties, Reynolds and Smith (1994) and Reynolds et al. (2002) developed an objective analysis algorithm to estimate SST by blending bias-adjusted satellite infrared SST retrievals in cloud-free regions with all available in situ measurements from ships and buoys while using information on locations of ice. Since few in situ observations exist over the expansive and infrequently traveled Southern Ocean, errors in the infrared satellite data generally persist into the estimated SST fields. Moreover, the advantages gained in the blending come at the expense of spatial resolution (Reynolds and Smith 1994).

Despite these shortcomings, the Reynolds SST analyses have been the best available estimate of the SST field over the Southern Ocean. Using these SST fields and surface wind stress measurements from the QuikSCAT scatterometer during the 2-yr period August 1999 to July 2001, OCE showed that surface winds were highly coupled to the underlying SST gradients over the entire Southern Ocean. Large uncertainties in the short-scale SST field estimated by the Reynolds SST analyses, however, limited the temporal resolution of the analysis in OCE to seasonal time scales. Additionally, as will be shown in section 3, the coarse spatial resolution of the Reynolds SST analyses led to a sub-

stantial underestimation of the SST gradients on the spatial scales that are important to the air–sea coupling that is of interest here.

In this paper, we use the AMSR SST measurements to develop a more detailed and accurate account of the coupling between SST and both wind stress and CLW over the 1-yr period 2 June 2002 to 7 June 2003, corresponding to the first complete year of the AMSR data record. The analysis region is 27° to 60°S, 0° to 100°E, encompassing the Agulhas Retroflexion and the Agulhas Return Current south of Africa. In the following section, the AMSR SST and CLW data, QuikSCAT wind data, and Reynolds SST analyses are described in detail. The differences between the Reynolds and AMSR SST fields are quantified in section 3. The coupling between SST and wind stress deduced from the AMSR and QuikSCAT observational data is summarized in section 4 and a brief discussion of the influence of surface-layer stability on the wind stress is presented in section 5. An analysis of the spatial and temporal variability of this coupling is presented in section 6, and an analysis and interpretation of spatial lags in the MABL response to SST forcing is presented in section 7. Observations of the CLW response are presented in section 8.

2. Data description

SST measurements from microwave satellite radiometers are not adversely affected by the ubiquitous cloud cover endemic to the Southern Ocean because nonprecipitating clouds are essentially transparent to microwave radiation. The first calibrated and accurate satellite microwave SST sensor was the Tropical Rainfall Measuring Mission (TRMM) Microwave Imager (TMI) (Wentz et al. 2000; Chelton et al. 2000). Because of the low inclination of the TRMM orbit, TMI measurements are restricted to the latitude range 38°N to 38°S, which leaves most of the Southern Ocean unsampled. Microwave SST measurements over the high-latitude Southern Ocean have only recently become available following the launch of the EOS *Aqua* satellite on 4 May 2002 and the initiation of the AMSR data record on 2 June 2002.

The AMSR measures horizontally and vertically polarized brightness temperatures at six microwave frequencies across a single 1445-km swath centered on the subsatellite ground track. SST, vertically integrated CLW, wind speed, vertically integrated water vapor, and rain rate are estimated over most of the global oceans from these 12 microwave brightness temperatures using physically based statistical regression (Wentz and Meissner 2000). The spatial resolution of the SST and CLW measurements utilized in this study

are 58 and 13 km, respectively. The SST and CLW measurements were averaged onto a 0.25° grid. Rain-contaminated estimates of SST and CLW were identified and excluded from further analysis based on collocated AMSR estimates of rain rate.

The accuracy of microwave SST retrievals has been evaluated through simulation studies (Wentz and Meissner 2000) and direct comparisons with in situ observations (Wentz et al. 2000). For a single observation, the rms SST accuracy is about 0.5°C. The random errors are further reduced here from consideration of weekly averages. Due to the lack of adequate in situ observations of CLW, the accuracy of the CLW retrieval can only be assessed through simulations and theoretical error models, which indicate an uncertainty of about 0.02 mm in units of precipitable water, or 20 g m⁻² in units of columnar-integrated liquid water density (Wentz and Meissner 2000).

In nonprecipitating weather conditions, the SeaWinds scatterometer onboard the QuikSCAT satellite infers the surface wind stress at a given location from microwave backscatter measurements of sea surface roughness obtained at multiple azimuths. The microwave backscatter is calibrated to the equivalent neutral stability wind at a height of 10 m above the surface, that is, the 10-m wind that would be associated with the observed wind stress if the atmosphere were neutrally stratified (Liu and Tang 1996). The vector wind stress τ was calculated from the 10-m neutral stability wind vector \mathbf{v}_{10}^N from the bulk formulation $\tau = \rho_0 C_d^N |\mathbf{v}_{10}^N| \mathbf{v}_{10}^N$, where ρ_0 is a constant surface air density and C_d^N is the neutral stability drag coefficient based on Large and Pond (1982) with a modification for low wind speeds suggested by Trenberth et al. (1990). The QuikSCAT wind stress fields were averaged onto the same 0.25° grid as the SST and CLW data. For each 0.25° grid cell, the weekly averaged QuikSCAT wind components were not used if precipitation occurred in five or more observations as determined from nearly coincident precipitation measurements made from a combination of four satellite microwave imagers, including the TMI and the Special Sensor Microwave Imagers (SSM/I) on the Defense Meteorological Satellite Program satellites F13, F14, and F15.

The 0.25°-gridded QuikSCAT winds and AMSR SST and CLW were averaged over weekly intervals. The QuikSCAT winds were further smoothed using a quadratic loess smoother (Cleveland and Devlin 1988; Schlax et al. 2001) with filter cutoff wavelengths of 2° latitude by 4° longitude, similar to the filtering properties of 1.2° latitude by 2.4° longitude block averages but with smaller filter sidelobes (see Fig. 1 of Chelton and Schlax 2003).

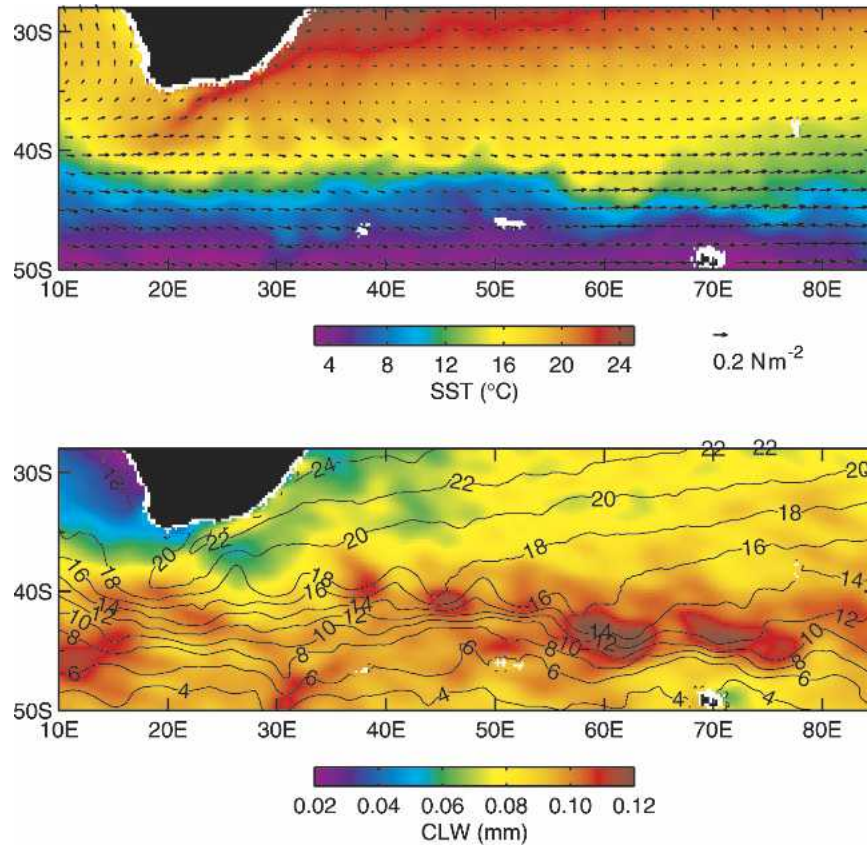


FIG. 1. Averages over the 1-yr period 2 Jun 2002 to 7 Jun 2003: (top) vector-averaged wind stress from QuikSCAT overlaid on AMSR SST; (bottom) CLW with contours of AMSR SST.

The weekly averaged wind stress, SST, and CLW fields south of the northernmost extent of the Antarctic ice edge were masked using ice fields constructed from AMSR brightness temperatures. In the weekly averaged data, 0.25° grid cells were flagged as ice contaminated when the AMSR measured ice 50% of the time or when the number of times that the AMSR identified a particular cell as containing ice exceeded the number of times the cell contained valid SST and CLW data. The maximum extent of ice cover during the 1-yr period analyzed here is shaded gray in the figures presented here.

The vector-averaged QuikSCAT wind stress over the 1-yr period 2 June 2002 to 7 June 2003 (Fig. 1, top) is predominately westerly over the ARC region. The maximum wind stress occurred between 45° and 50° S with a magnitude exceeding 0.25 N m^{-2} . This corresponds to a wind speed exceeding 11 m s^{-1} , which is among the largest annual mean wind speed anywhere in the world oceans. The 1-yr average SST measured by the AMSR is shown in color in the top panel of Fig. 1. Wind blowing across the meandering SST isotherms associated with the ARC makes this an ideal region to

investigate the influence of SST on the wind stress, wind stress curl and divergence, and CLW.

The 1-yr average CLW is shown in Fig. 1 (bottom) with SST contours overlaid. Large values of mean CLW occur between 40° and 50° S in association with the frequent growth and passage of synoptic scale weather systems and the close proximity of the ARC to the Southern Hemisphere atmospheric polar front (Peixoto and Oort 1992). Poleward of this maximum, CLW decreases because colder atmospheric columns tend to hold less precipitable water. Equatorward of this maximum, large-scale subsidence in the subtropics is unfavorable for deep cloud formation, limiting CLW to smaller values. Spatial variability in the 1-yr average CLW is mainly attributable to variability in precipitable water and cloud forcing mechanisms that determine cloud type and thickness.

The meanders in the ARC evident in the 1-yr average AMSR SST coincide with prominent bathymetric features. The ARC is intersected by the Agulhas Plateau, the Mozambique Escarpment, the Southwest Indian Ridge, and the Kerguelen Plateau (Fig. 2). Most of these features rise to within 2000 m of the surface, di-

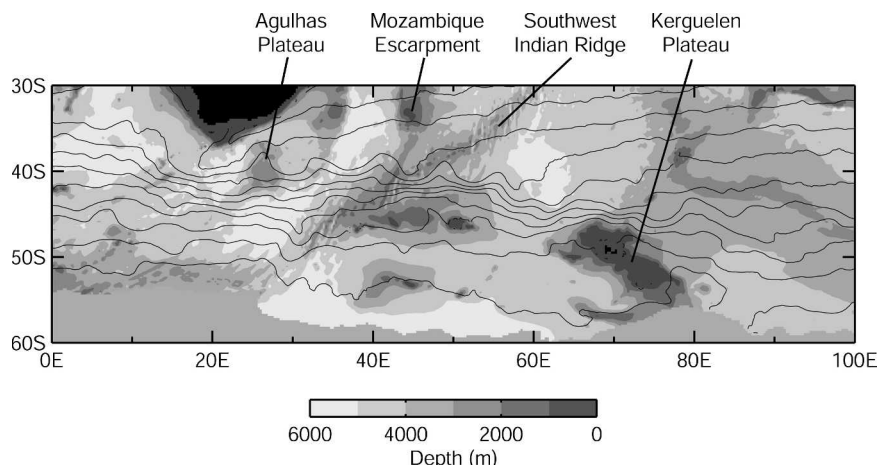


FIG. 2. Map of the bathymetry and geographical locations of major bathymetric features in the Agulhas Return Current region (shaded) with contours of the 1-yr average AMSR SST as shown in Fig. 1 overlaid. The gray shade bar at the bottom of the map indicates the range of water depth.

rectly influencing the ARC surface flow (Lutjeharms and van Ballegooyen 1984).

3. Comparison between AMSR and Reynolds SST

In our previous study of air–sea coupling over the Southern Ocean (OCE), we used the Reynolds SST analyses during the 2-yr period August 1999 to July 2001 (i.e., prior to the 2 June 2002 beginning of the AMSR data record). The Reynolds analyses of weekly averaged SST on a 1° spatial grid are produced by the National Oceanic and Atmospheric Administration (NOAA) using a blending of in situ and bias-adjusted satellite infrared data as described by Reynolds and Smith (1994) and Reynolds et al. (2002). The satellite infrared SST measurements are from the Advanced Very High Resolution Radiometer (AVHRR) onboard the NOAA series of polar-orbiting satellites. Microwave SST observations from the TMI and AMSR are not presently included in the Reynolds SST analyses. The coarse resolution of the Reynolds SST fields is quantified in this section by comparisons with AMSR SST fields.

The mean Reynolds SST and SST gradient fields over the 1-yr period 2 June 2002 to 7 June 2003 (Figs. 3b and 3d) capture the main features in the ARC, but with much less detail than in the AMSR SST field (Figs. 3a and 3c). In the 1-yr average AMSR SST gradient field (Fig. 3c), the ARC SST front is twice as intense as in the Reynolds SST (Fig. 3d). The much higher spatial resolution of the AMSR SST is clearly evident from the detailed structure of the meanders in the ARC that remained essentially stationary over the 1-yr period analyzed here. Boebel et al. (2003) has previously ob-

served that these meanders in the ARC are nearly stationary from an analysis of three years (1997–99) of merged sea surface height data from the TOPEX/Poseidon and ERS altimeters.

Of particular interest in this study are the small-scale features in the AMSR SST field. These were obtained by first isolating the large-scale SST fields by applying a loess filter with half-power filter cutoff wavelengths of 10° latitude by 30° longitude, roughly equivalent to 6° latitude by 18° longitude block averages. The spatially high-pass filtered fields were then obtained by subtracting the loess smoothed fields from the unsmoothed SST fields. The resulting 1-yr average high-pass filtered SST fields are shown in Fig. 4 (top) as contours overlaid on the spatially high-pass filtered QuikSCAT wind stress magnitude. The spatially high-pass filtered fields analyzed throughout this study are referred to hereafter as perturbation fields. The high spatial correlation of 0.83 between the 1-yr average perturbation AMSR SST field and the 1-yr average perturbation QuikSCAT wind stress magnitude (upper panel of Fig. 4) is consistent with the earlier observations of SST influence on surface winds summarized in section 1. The spatial correlation between 1-yr averages of the perturbation Reynolds SST field and the perturbation QuikSCAT wind stress magnitude (bottom panel of Fig. 4) is only 0.65.

In addition to the lower correlation between the Reynolds SST fields and the overlying wind fields, it is apparent from Fig. 4 that the intensities of the short-scale perturbations in the Reynolds SST field are significantly underestimated because of the inherently coarse spatial resolution of the Reynolds SST analyses.

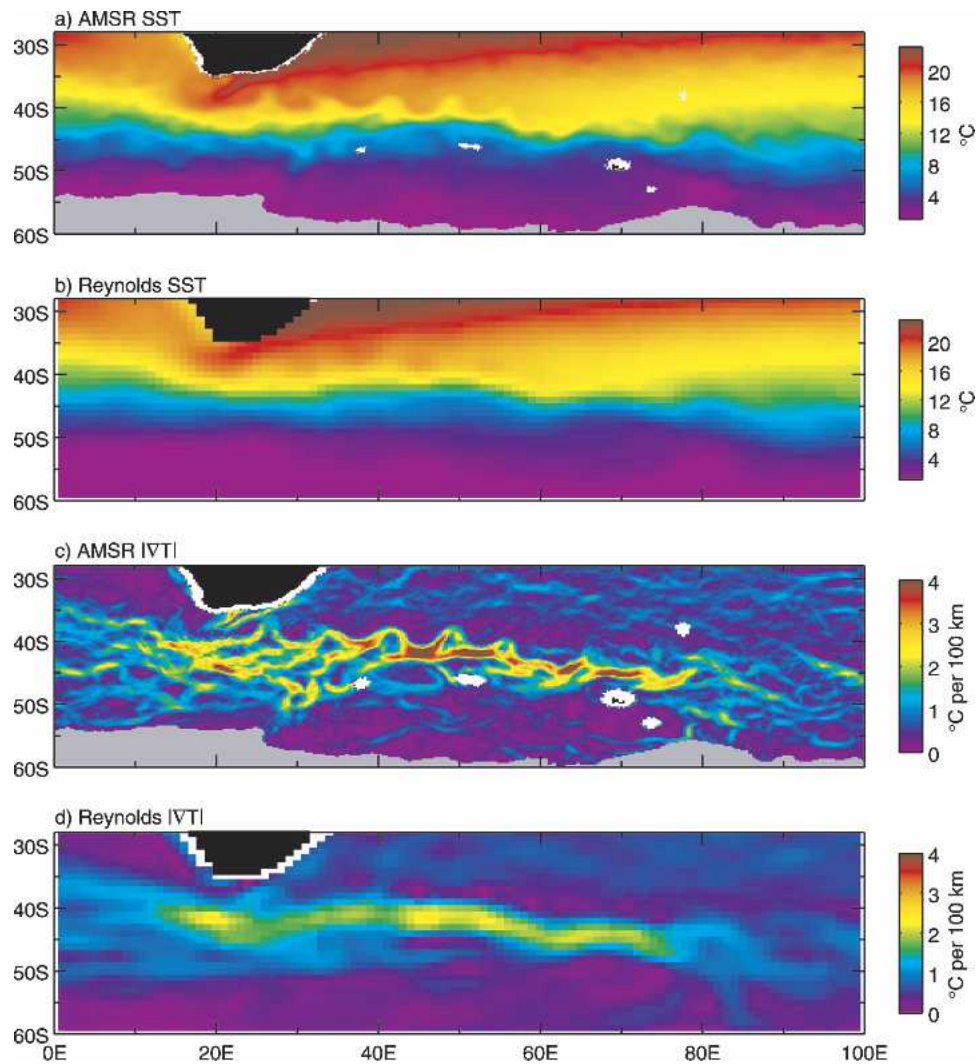


FIG. 3. Maps of (a) AMSR SST, (b) Reynolds SST, (c) AMSR SST gradient magnitude, and (d) Reynolds SST gradient magnitude, averaged over the 1-yr period 2 Jun 2002 to 7 Jun 2003. Regions containing any sea ice during the 1-yr period are shown in gray in (a) and (c).

The weak short-scale SST gradients in the Reynolds analyses are statistically quantified in Fig. 5. The short-scale SST gradient magnitudes computed from the Reynolds analyses are, on average, about a factor of 5 smaller than those computed from the AMSR SST (Fig. 5, top). The distribution of the perturbation SST gradient magnitudes for the Reynolds SST (Fig. 5, bottom) has a dynamic range that is only about half that of the AMSR. The superiority of the AMSR SST fields for investigation of SST influence on the winds and clouds in the ARC region is thus apparent.

4. Coupling between the wind stress and SST fields

The total SST gradient vector in Cartesian coordinates can be decomposed into local crosswind and

downwind components. In vector notation, these are the cross product $\nabla T \times \hat{\tau} = |\nabla T| \sin \theta$ and the dot product $\nabla T \cdot \hat{\tau} = |\nabla T| \cos \theta$, where $\nabla = \mathbf{i}\partial/\partial x + \mathbf{j}\partial/\partial y$ is the two-dimensional gradient operator in Cartesian coordinates with unit vectors \mathbf{i} and \mathbf{j} in the zonal and meridional directions, respectively, T is the SST, $\hat{\tau}$ is a unit vector in the direction of the wind stress, and θ is the counterclockwise angle between the vectors ∇T and $\hat{\tau}$. When the surface wind blows obliquely across a SST front, the crosswind component of the SST gradient is nonzero. A lateral (crosswind) gradient of the wind develops because the wind speed is higher over the warmer water, resulting in a curl of the wind. Similarly, a downwind component of the SST gradient is associated with a longitudinal (downwind) deceleration or acceleration of the wind across the SST front, resulting

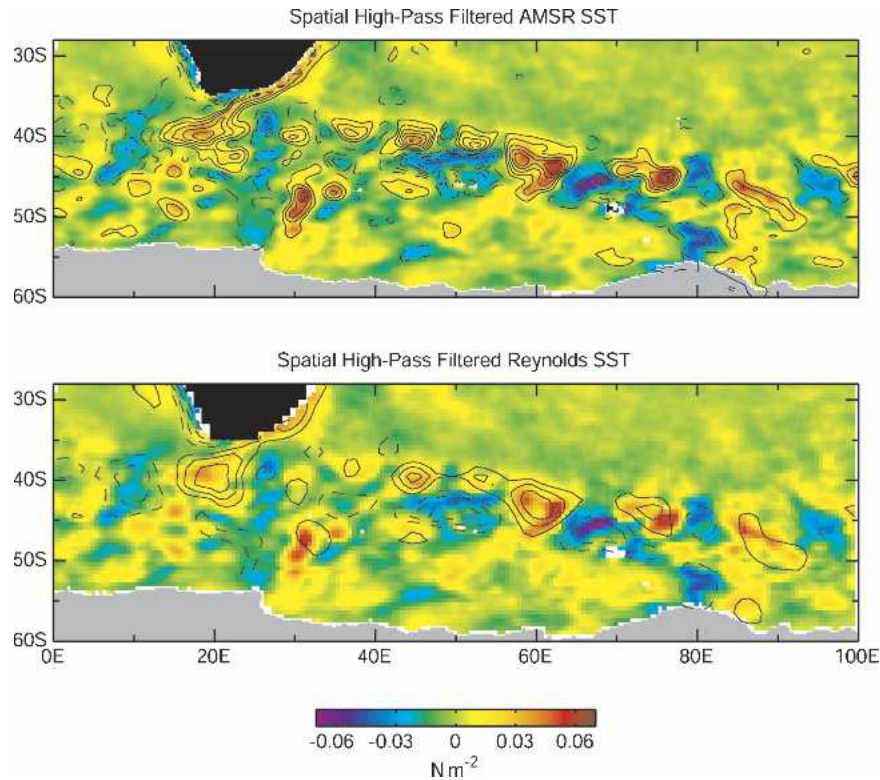


FIG. 4. Maps of the perturbation wind stress magnitude from QuikSCAT averaged over the 1-yr period 2 Jun 2002 to 7 Jun 2003 shown in color. The overlaid contours are of the perturbation (top) AMSR SST and (bottom) Reynolds SST with a contour interval of 0.5°C . Dashed and solid contours in each panel correspond to negative and positive SST perturbations, respectively, and the zero contour has been omitted for clarity. The spatial high-pass filtering used to obtain these perturbation fields attenuates features with wavelengths longer than 10° latitude by 30° longitude.

in a convergence or divergence of the low-level winds. The wind stress curl and divergence should therefore depend respectively on the crosswind and downwind SST gradients (see Fig. 3 of OCE).

SST-induced perturbations of the wind stress curl field are masked somewhat by the background curl of the large-scale mean wind field. In the ARC region that is the focus of this study, the large-scale wind stress curl is respectively positive and negative to the north and south of the westerly wind maximum located along approximately 45°S . The wind stress curl perturbations induced by crosswind SST gradients associated with the perturbation SST field were isolated by subtracting the 10° latitude by 30° longitude loess-smoothed curl field from the unsmoothed curl field (Fig. 6, bottom). The short-scale curl field is most intense along the ARC just south of 40°S , coincident with the largest perturbation crosswind SST gradients associated with the ARC (contours in the bottom panel of Fig. 6). These persistent SST-induced short-scale perturbations in the curl field from the steady meanders in

the SST front have magnitudes comparable to the large-scale curl field. The associated Ekman pumping (see Fig. 8 of OCE) likely has significant regional implications for the upper ocean circulation along the ARC.

The 1-yr average wind stress divergence is shown in Fig. 7 (top). Like the curl, the divergence is most spatially variable over a band centered on the ARC. The spatial high-pass filtered wind stress divergence field obtained by the same filtering procedure applied to the wind stress curl is shown in the bottom panel of Fig. 7. The large-scale divergence field is quite small as a consequence of the tendency for the mean wind stress field to be nondivergent. The unfiltered and spatially high-pass filtered divergence fields therefore differ by relatively little when compared to the differences between the unfiltered and spatially high-pass filtered curl fields. Positive and negative perturbations form in the divergence field over positive and negative perturbation downwind SST gradients (contours in the bottom panel of Fig. 7) associated with meanders in the ARC.

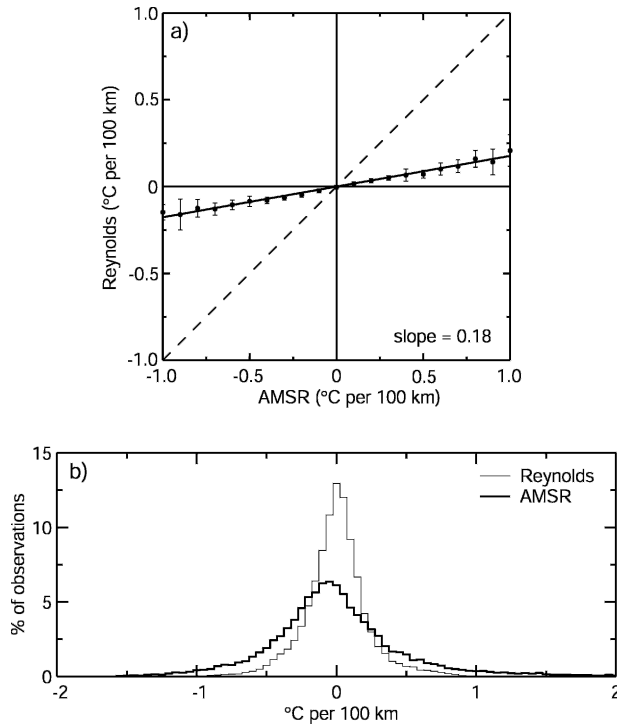


FIG. 5. (a) Binned scatterplot of the Reynolds perturbation SST gradient magnitude as a function of the AMSR perturbation SST gradient magnitude. The points represent the means within each bin computed from 17 overlapping 6-week averages over the 1-yr period from 2 Jun 2002 to 7 Jun 2003, and the error bars are ± 1 std dev of the means within each bin. The line through the points represents a least squares fit of the binned overall means to a straight line and the dashed line with unit slope is shown for reference; (b) histograms of the perturbation SST gradient magnitude computed from the Reynolds analyses (thin solid line) and AMSR (thick solid line) over the 17 individual 6-week averages. For both panels, the AMSR SST gradients were computed after block averaging the AMSR data onto the same $1^\circ \times 1^\circ$ spatial grid as the Reynolds analyses.

While the 1-yr average maps in Figs. 6 and 7 illustrate the mean properties of the wind stress curl and divergence fields over the ARC, it is desirable to average over shorter time periods for statistical analysis of the coupling between SST and the wind stress field. Energetic synoptic-scale frontal disturbances in this region conceal SST-induced perturbations in the wind stress and wind stress derivative fields constructed with short temporal averaging. The effects of weather disturbances were mitigated in OCE by block averaging the wind stress and SST data over 3-month periods. The choice of a 3-month averaging period was chosen primarily to abate concerns about the accuracy of the Reynolds SST analyses in shorter time averages over the sparsely sampled Southern Ocean. The dense coverage and high spatial resolution and accuracy of the AMSR SST data obviate such concerns.

The averaging period required to reduce the effects of weather variability was investigated from the cross correlation between the QuikSCAT perturbation wind stress magnitude and the perturbation AMSR SST as a function of the block averaging period from the first 53 weeks of AMSR data. The cross correlation increases rapidly from 0.5 in weekly averages to more than 0.7 for averaging periods longer than 4 weeks, as shown by the dots in Fig. 8. The cross correlations with the Reynolds SST (shown by squares in Fig. 8) increase more slowly with increasing averaging period and are smaller for all averaging periods, presumably because of inaccuracies in the Reynolds SST fields, due at least in part to the spatial and temporal smoothing in the Reynolds analyses (see section 3).

On the basis of Fig. 8, the data were averaged into 17 overlapping 6-week blocks at 3-week intervals for the statistical analyses in this study. The 10° latitude by 30° longitude spatial high pass filtering was applied to each of the overlapping 6-week average wind stress magnitude, curl, divergence, SST, and the crosswind and downwind SST gradient fields. These filtered fields are denoted respectively as $|\tau'|$, $\nabla \times \tau'$, $\nabla \cdot \tau'$, T' , $(\nabla T \times \hat{\tau})'$, and $(\nabla T \cdot \hat{\tau})'$.

The spatially high-pass filtered crosswind and downwind components of the SST gradient can be written as

$$(\nabla T \times \hat{\tau})' = |\nabla T'| \sin \theta' \quad (1)$$

$$(\nabla T \cdot \hat{\tau})' = |\nabla T'| \cos \theta', \quad (2)$$

from which it is seen that the angle θ' is defined by

$$\theta' = \tan^{-1} \left[\frac{(\nabla T \times \hat{\tau})'}{(\nabla T \cdot \hat{\tau})'} \right]. \quad (3)$$

To investigate the hypothesis that the spatially high-pass filtered wind stress curl and divergence fields over the ARC are functions of $(\nabla T \times \hat{\tau})'$ and $(\nabla T \cdot \hat{\tau})'$, respectively, $\nabla \times \tau'$ and $\nabla \cdot \tau'$ were binned as functions of θ' for each of the overlapping 6-week block averages. The overall averages within each bin are shown as points in Fig. 9. As previously shown for the Southern Ocean by OCE and for the eastern tropical Pacific by Chelton et al. (2001), the QuikSCAT perturbation curl and divergence fields agree remarkably well with sine and cosine dependencies on θ' . The short-scale features in the curl and divergence fields thus depend respectively on the perturbation crosswind and downwind components of the SST gradient.

An interesting feature in the angular dependencies of the curl and divergence is the small phase shift relative to pure sine and cosine functions, respectively. A similar phase shift for the divergence but not for the curl was noted by OCE from SST gradients computed from

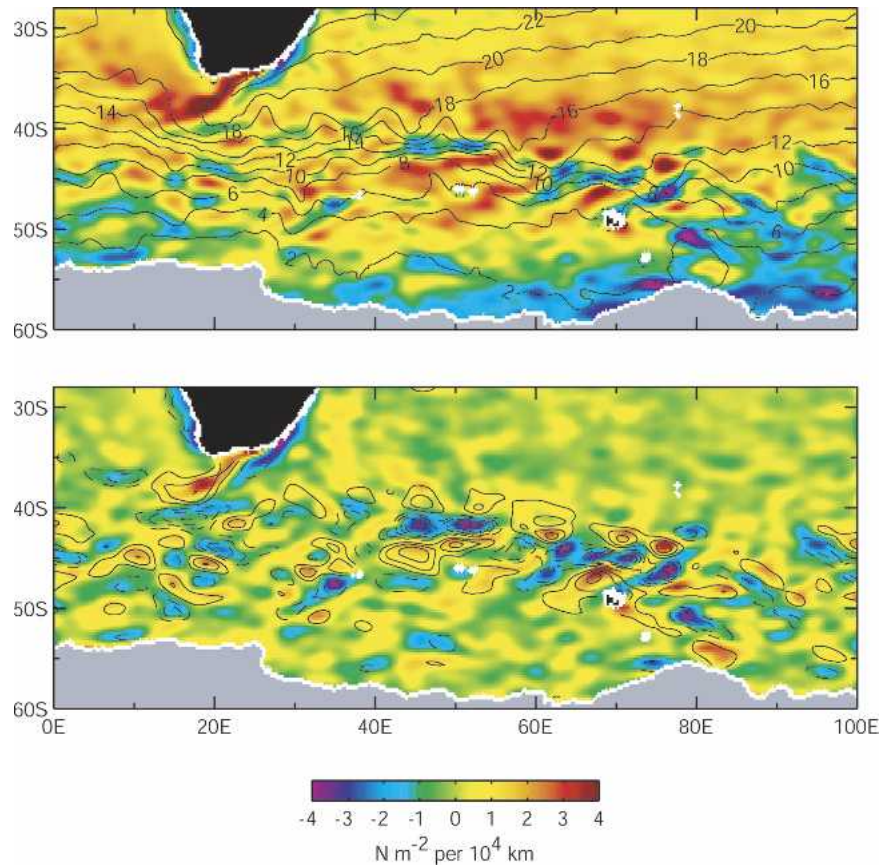


FIG. 6. Maps of the wind stress curl averaged over the 1-yr period 2 Jun 2002 to 7 Jun 2003 from QuikSCAT of (top) 2° latitude by 4° longitude loess-smoothed fields of wind stress curl (color) and SST (contours); and (bottom) 30° longitude by 10° latitude spatially high-pass-filtered fields of wind stress curl (color) and the crosswind SST gradient [contours, with a contour interval of $0.3^\circ\text{C} (100\text{ km})^{-1}$]. Dashed and solid contours in the bottom panel correspond to negative and positive crosswind SST gradients, respectively, and the zero contour has been omitted for clarity.

the Reynolds SST analyses. The lack of evidence for a phase shift in the curl fields was evidently because of the coarse resolution and perhaps inaccuracies in the Reynolds SST fields used in that study. Though small, we believe that the phase shifts in Fig. 9 for the ARC region are statistically significant. They may be an indication of the importance of SST-induced perturbations of the pressure gradient on the cross-frontal flow of low-level winds (Lindzen and Nigam 1987; Cronin et al. 2003; Small et al. 2005). This is a subject of ongoing analysis.

The wind stress curl and divergence responses to a given SST gradient can be determined by binning $\nabla \times \tau'$ and $\nabla \cdot \tau'$ as functions of $(\nabla T \times \hat{\tau})'$ and $(\nabla T \cdot \hat{\tau})'$, respectively. As shown in Fig. 10, the perturbation curl and divergence over the ARC are linearly related to the perturbation crosswind and downwind SST gradients, respectively, consistent with the mechanisms discussed

in the introduction and the results obtained by OCE for the entire Southern Ocean. The magnitude of the response between the derivative wind stress fields and the SST gradient components is given by the slopes of the lines in Fig. 10, denoted here as α_C for the curl and α_D for the divergence.

The coupling coefficients α_C and α_D calculated here are larger than those calculated by OCE by factors of 3 and 2, respectively. Some of the stronger responses obtained from this study are due to the differences between the ARC region considered here and the entire Southern Ocean considered by OCE. An analysis of QuikSCAT and AMSR data performed over the entire Southern Ocean (not shown here) indicates that the magnitude of the coupling coefficients are about 20% larger for the ARC region. Most of the differences between the values of α_C and α_D obtained here and the values obtained in OCE are evidently due to errors in

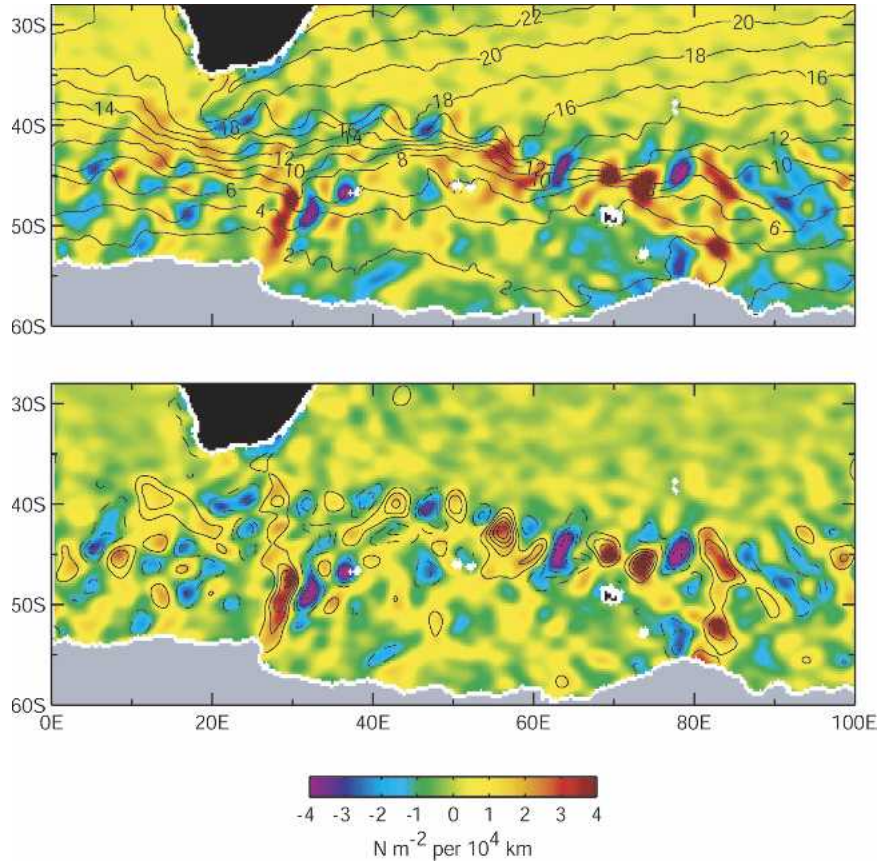


FIG. 7. As in Fig. 6 except for the wind stress divergence and downwind SST gradient [contours; with a contour interval of $0.3^{\circ}\text{C} (100 \text{ km})^{-1}$]. Dashed and solid contours in the bottom panel correspond to negative and positive downwind SST gradients, respectively, and the zero contour has been omitted for clarity.

the location and magnitude of SST gradients in the Reynolds SST analyses used in OCE. It is also noteworthy that the standard deviations within each bin in Fig. 10 are much smaller than those obtained by OCE, evidently due to the greater accuracy of the AMSR SST fields compared with the Reynolds SST analyses.

5. Surface layer stability effects on the wind stress

The effects of surface layer stability alone on the surface wind stress can be isolated by investigating the stability dependence of the drag coefficient C_D over warm and cool water. The change in wind stress magnitude $\Delta|\tau|$ caused only by changes in the stability-dependent drag coefficient ΔC_D can be calculated as

$$\Delta|\tau| = \rho_0|\mathbf{U}|^2\Delta C_D, \tag{4}$$

where $|\mathbf{U}|$ is the wind speed, which is considered constant for the purposes of this sensitivity analysis. Here

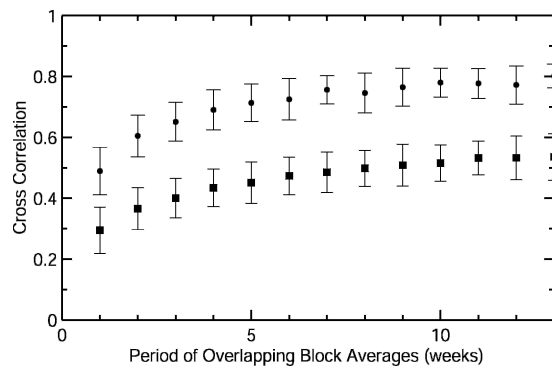


FIG. 8. Binned scatterplot of the cross correlation between the perturbation wind stress magnitude from QuikSCAT and the perturbation SST as a function of averaging period. The round dots are for the AMSR SST and the squares are for the Reynolds SST. The points represent the mean cross correlation within each bin computed from the maximum number of overlapping block averages at weekly intervals possible within the 1-yr period 2 Jun 2002 to 7 Jun 2003. The error bars represent ± 1 std dev about the means within each bin.

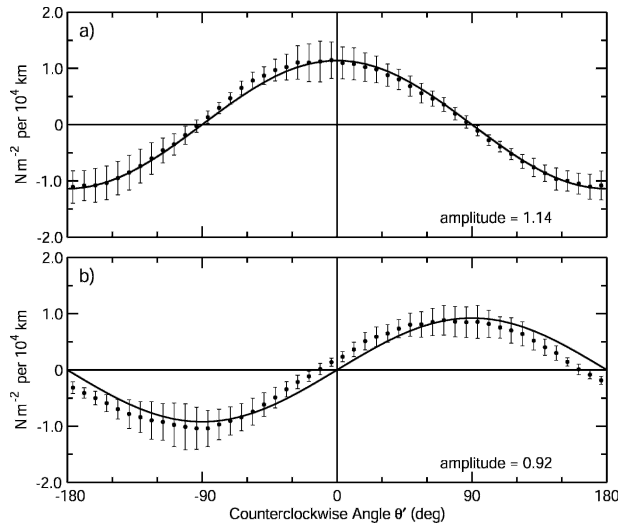


FIG. 9. Binned scatterplots of the angular dependencies of (a) the perturbation wind stress divergence and (b) the perturbation wind stress curl on the angle θ' defined by Eq. (3). The points in (a) and (b) are the means within each bin computed from 17 overlapping 6-week averages over the 1-yr analysis period, and the error bars represent ± 1 std dev of the means within each bin. The solid curves in (a) and (b) represent least squares fits to a cosine and a sine, respectively.

C_D was calculated separately over the warm and cool water using the surface layer similarity relation

$$C_D = \left[\frac{k}{\ln(z/z_0) - \Psi_M(\zeta)} \right]^2, \quad (5)$$

where k is the von Kármán constant, Ψ_M is a surface layer stability correction function for momentum (Stull 1988), $\zeta = z/L$ is the nondimensional height, z is the measurement height of 10 m, L is the Obukhov length scale, and z_0 is the roughness length.

To investigate the sensitivity of $\Delta|\tau|$ to ΔC_D , we consider a broad range of ζ over the ocean from -0.3 in unstable convective boundary layers over warm SST perturbations to 0.3 in stable boundary layers over cool SST perturbations, corresponding to surface buoyancy fluxes of about $\pm 70 \text{ W m}^{-2}$. This range of surface buoyancy fluxes is generally much larger than the range contained, for example, in 1-yr averages of buoyancy fluxes estimated from the National Centers for Environmental Prediction (NCEP) reanalysis over the Agulhas Return Current. The effects of stability in reality are therefore smaller than those considered here. For an 8 m s^{-1} incident wind over the ocean, z_0 is about $2 \times 10^{-4} \text{ m}$ by Charnock's relation. The resulting ΔC_D between warm and cool SST perturbations is thus about 4×10^{-4} , leading to a $\Delta|\tau|$ of about 0.03 N m^{-2} . The cross-frontal wind stress variations caused by stability-dependent

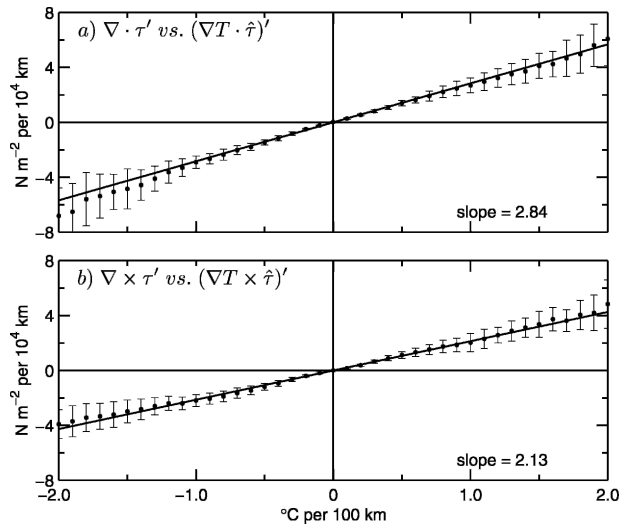


FIG. 10. Binned scatterplots of the relationships between the perturbation SST and wind stress fields: (a) the perturbation divergence plotted as a function of the perturbation downwind SST gradient; (b) the perturbation wind stress curl plotted as a function of the perturbation crosswind SST gradient. The points in (a) and (b) are the means within each bin computed from the 17 individual overlapping 6-week averages, and the error bars are ± 1 std dev of the means within each bin. The lines through the points represent least squares fits to straight lines.

variations in C_D are less than a third of the typical observed differences of more than 0.1 N m^{-2} over the Agulhas Return Current as shown in the top panel of Fig. 4. A more realistic range of ζ from -0.3 over warm water to 0 (neutral stability) over cool water yields a wind stress difference of only about 0.01 N m^{-2} , which is an order of magnitude smaller than the observed perturbations. We therefore conclude that cross-frontal variations in C_D alone cannot explain the observed cross-frontal variations in wind stress.

6. Spatial and temporal variability of the ocean-atmosphere coupling

Although the 1-yr record of the AMSR data used in this study limits the investigation of temporal variability, there is strong seasonal variability in the curl and divergence response to SST (thick lines in Fig. 11). The coupling coefficients α_C and α_D calculated from the AMSR SST fields increase by 100% and 75%, respectively, during the wintertime compared to the summertime. While the magnitudes of α_C and α_D computed from the Reynolds SST fields are much smaller than those computed from the AMSR SST fields as discussed in section 4, the 4-yr record of α_C and α_D calculated from the QuikSCAT wind stress and Reynolds

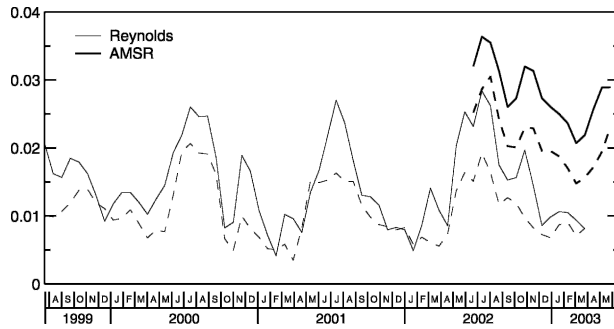


FIG. 11. Time series of the coupling coefficients α_C (dashed lines) and α_D (solid lines) calculated from the overlapping 6-week block averages. The thick and thin lines represent the coupling coefficients calculated from the AMSR and Reynolds SST fields, respectively.

SST fields reveals a well-defined seasonal cycle with maxima during July and minima during December and January (thin lines in Fig. 11). The surface wind stress response to SST perturbations is thus significantly stronger during the austral winter than during the summer.

The observed seasonal cycle of the coupling coefficients are likely related to large-scale seasonal variability in the depth of the MABL. In this case, one would expect the seasonal cycles of the coupling coefficients and MABL depth to be related through the effects of seasonal variations of surface heat flux and stratification of the lower troposphere. An overall decrease in ambient static stability during the wintertime because of cooler air aloft relative to the air near the sea surface would allow deeper turbulent and convective mixing of momentum and heat.

A quantitative test of the above hypothesized mechanism for the observed seasonal cycle of the coupling coefficients would require detailed information about the vertical structure of the MABL. Such information is not available from observations. The surface sensible heat fluxes and atmospheric temperature fields from the NCEP reanalyses (Kalnay et al. 1996) provide at least some insight into the processes involved. Although the vertical resolution of the NCEP fields is coarse, the vertical potential temperature gradient between 700 and 1000 hPa, $\partial\theta_p/\partial z$, where θ_p is the potential temperature, provides a rough measure of the stratification of the lower troposphere.

The first empirical orthogonal functions and associated amplitude time series of the monthly averaged surface sensible heat flux and the stratification are shown in Figs. 12 and 13. The surface sensible heat flux is maximum and the stratification is minimum during the winter. Likewise, the surface sensible heat flux is minimum and the stratification is maximum during the sum-

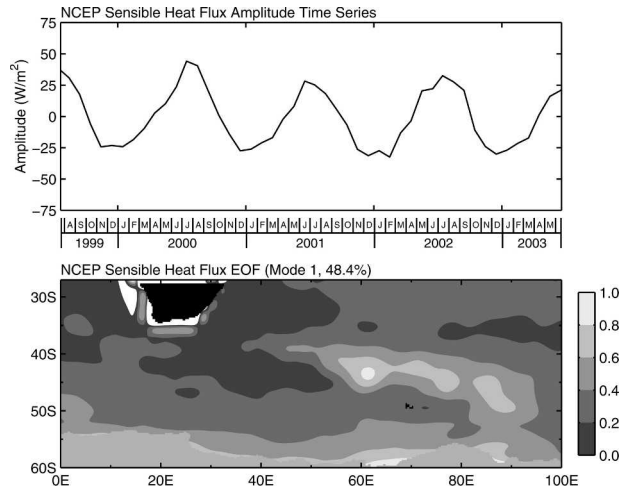


FIG. 12. (top) First mode amplitude time series and (bottom) the corresponding empirical orthogonal function of the NCEP surface sensible heat flux over the time period from Aug 1999 to May 2003.

mer. The large-scale lower troposphere over the ARC is therefore less convectively stable during the winter than during the summer.

The correspondence between the intensity of the ocean–atmosphere coupling and stratification is evident from the geographic variability of α_C and α_D . Values of α_C and α_D were calculated for 3° latitude by 5° longitude regions using the 17 overlapping 6-week averaged fields. The magnitudes of the coupling coefficients vary considerably latitudinally, with maxima located along a band centered between about 40° and 50° S latitude (Fig. 14). The small values of the coupling coefficients outside of this band are mainly due to a low signal-to-

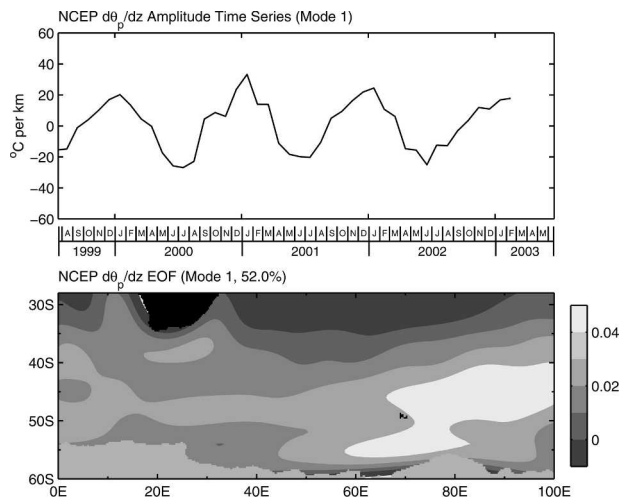


FIG. 13. As in Fig. 12, except for the NCEP potential temperature lapse rate, $\partial\theta_p/\partial z$.

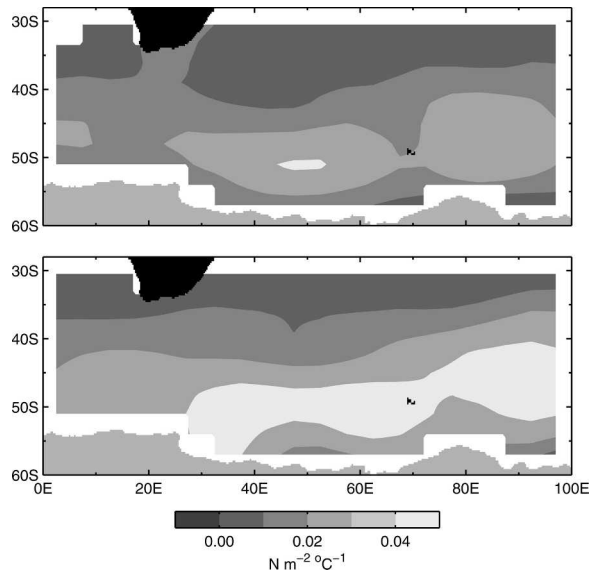


FIG. 14. Spatial maps of the coupling coefficients (top) α_C and (bottom) α_D averaged over the 1-yr period 2 Jun 2002 to 7 Jun 2003.

noise ratio; however, α_C and α_D vary geographically by about a factor of 3 within the band of significant short-scale curl and divergence variability. This relationship is statistically quantified by bin averaging $\partial\theta_p/\partial z$ as a function α_C and α_D as shown in the top and bottom panels of Fig. 15. It is evident from these bin averages that the coupling coefficients increase with increasing tropospheric stability. This is consistent with the hypothesis that stratification plays an important role in

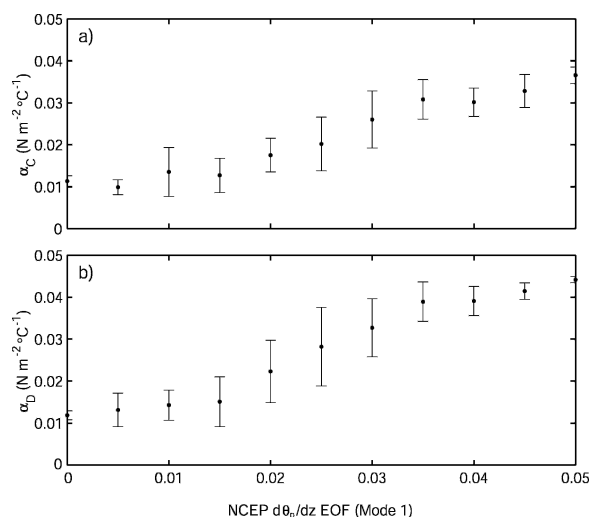


FIG. 15. Binned scatterplots of the relationships between the NCEP potential temperature lapse rate ($\partial\theta_p/\partial z$) and the coupling coefficients (top) α_C and (bottom) α_D .

determining the surface wind stress response to a given SST gradient.

Another possible mechanism for the observed seasonal variability of α_C and α_D is seasonal variability of the near-surface flow caused by ageostrophic cross-frontal pressure gradients over regions of large SST gradients. These pressure gradients owe their existence to spatial variations in MABL depth and vertical thermal structure (Lindzen and Nigam 1987; Hashizume et al. 2002; Small et al. 2003, 2005) across the SST front. Seasonal variability in the large-scale MABL depth and thermal structure could thus contribute to the seasonal cycle of the coupling coefficients. Few observations of the seasonal cycle of these variables exist to test this hypothesis over the ARC. An analysis of archived radiosonde data (not shown here) available from four island weather stations scattered within the geographical region considered here was inconclusive in determining whether seasonal variability in large-scale MABL depth and thermal structure could account for the observed seasonal variability in the coupling coefficients.

Cronin et al. (2003) found that sea level pressure perturbations associated with tropical instability waves in the eastern tropical Pacific have a magnitude of about 0.1 hPa per $^{\circ}\text{C}$ SST change. Wai and Stage (1989) found nearly the same magnitude of SST-induced pressure perturbations from a 2-dimensional mesoscale atmospheric model of the MABL response to SST over the Gulf Stream. We are not confident that the NCEP reanalyses are sufficiently accurate to investigate the importance of such small pressure changes to the wind field in the ARC region of interest in this study.

7. Spatial lags in the SST-induced MABL response

On close inspection, a consistent, but small, downwind lag is visually evident in the bottom panels of Figs. 6 and 7 where local extrema of the perturbation curl and divergence consistently occur slightly downwind of local extrema of the perturbation crosswind and downwind SST gradients. A maximum correlation of 0.86 occurs when the perturbation divergence is lagged 0.25° to the east (i.e., downwind in this region of westerly winds) of the perturbation downwind SST gradient (Fig. 16, top). This is consistent with the notion that the surface winds do not adjust instantaneously to changes in MABL stability as the large-scale winds advect air across SST perturbations. The downwind lag depends on the MABL adjustment and advective time scales. The downwind lag of 0.25° is small in comparison with the characteristic length scale of SST and wind stress perturbations over the ARC.

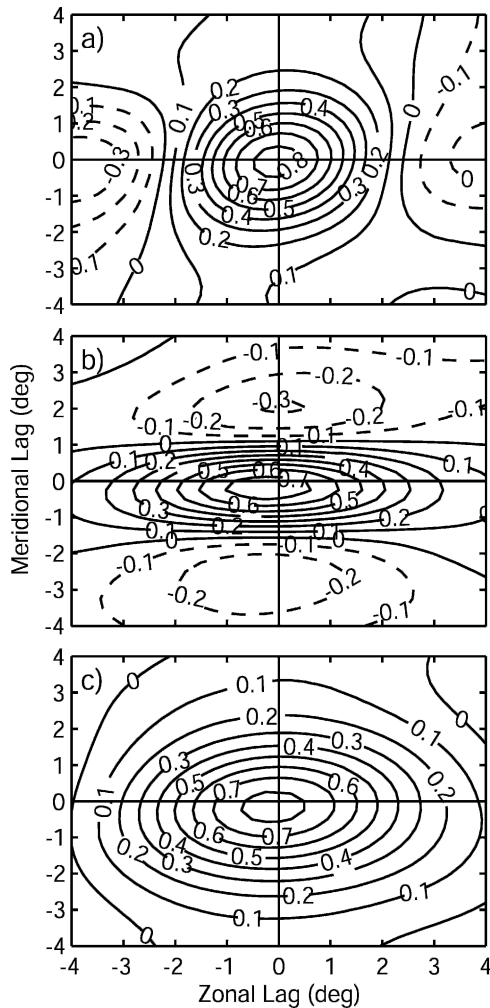


FIG. 16. Spatial-lagged cross correlations between 1-yr average perturbations: (a) downwind SST gradient and wind stress divergence; (b) crosswind SST gradient and wind stress curl; (c) SST and wind stress magnitude. Negative meridional (zonal) lags indicate that SST perturbations are lagged to the south (west) of wind stress perturbations.

The spatial-lagged cross correlation between the 1-yr average perturbation curl and crosswind SST gradient is shown in the middle panel of Fig. 16. A maximum cross correlation of 0.78 occurs when the perturbation curl is lagged 0.25° to the east and 0.25° to the north of the perturbation crosswind SST gradient. A similar lag structure is observed in the spatial-lagged cross correlation between the 1-yr average perturbation wind stress magnitude and SST (bottom panel of Fig. 16); a maximum correlation of 0.84 occurs when the perturbation wind stress magnitude is lagged 0.25° to the east and 0.25° to the north of the perturbation SST. While the zonal lag is probably the result of the same processes that are responsible for the lag in the perturba-

tion divergence in Fig. 16 (top), this cannot explain the meridional lag.

The 0.25° meridional shift in the maximum responses of the curl and wind stress magnitude to SST suggests a link to the approximately zonal surface velocity of the ARC. Strong surface ocean currents have a measurable effect on scatterometer wind stress because scatterometers measure the actual stress on the moving sea surface rather than relative to a stationary sea surface (Cornillon and Park 2001; Kelly et al. 2001; Chelton et al. 2001). Because of the quasigeostrophic and nondivergent nature of ocean currents, the effects of the currents on the stress are manifest in the wind stress curl but not in the wind stress divergence (Chelton et al. 2004). Since the ocean surface currents are expected to be strongest along the SST front, there is a positive (negative) curl of the surface currents north (south) of the front. The true wind stress curl that is measured by QuikSCAT is thus displaced northward relative to its position if the water surface were not moving, consistent with the meridional lag observed in Fig. 16.

A quantitative test of this hypothesis requires knowledge of the surface ocean currents. Direct surface current observations do not exist in the ARC over the time and space scales under consideration here and surface velocities from ocean circulation models have not been demonstrated to be quantitatively accurate enough to use as surrogate estimates of the currents. To investigate the effects of ocean currents, the geostrophic surface velocity was estimated from the AMSR SST as follows. The relationship between SST and dynamic height relative to 1000 m over the ARC was determined by regression analysis from climatological hydrographic data (Levitus and Boyer 1994). The dynamic height was found to be linearly related to SST over the Agulhas region with a correlation coefficient of 0.98 and a slope of $0.053 \text{ m } ^\circ\text{C}^{-1}$. Weekly averages of the dynamic height fields were estimated from the weekly averaged AMSR SST fields using this linear relation. The geostrophic surface ocean velocity was then estimated from the gradient of the dynamic height field. The typical computed geostrophic current velocity along the SST front is about 50 cm s^{-1} , which is at least qualitatively consistent with the geostrophic velocities computed by Lutjeharms and Ansorge (2001).

The wind stress and wind stress curl and divergence that would exist in the absence of surface ocean currents were estimated by adding the regression estimates of the geostrophic surface currents to the scatterometer winds. The spatial-lagged cross correlation of the resulting fields are shown in Fig. 17. The meridional lag vanishes in the adjusted perturbation wind stress curl and wind stress magnitude fields, suggesting a nexus

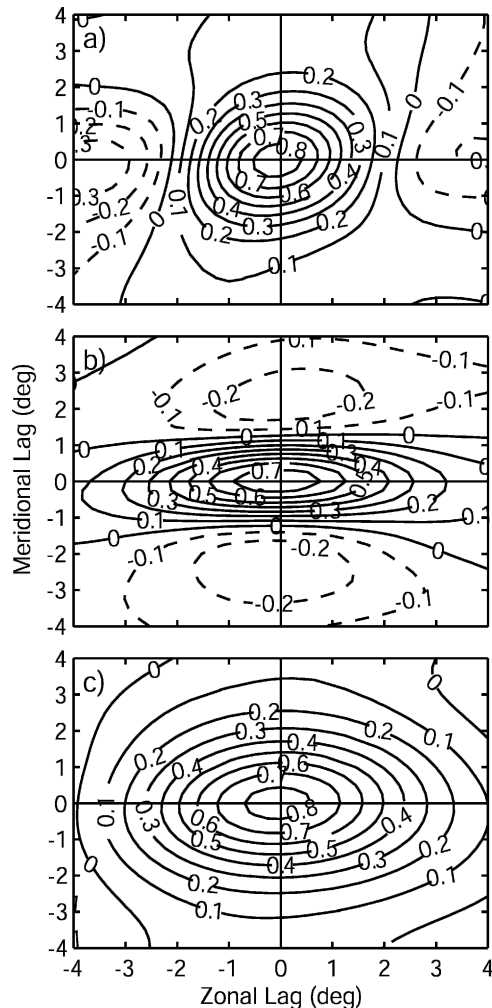


FIG. 17. As in Fig. 16 except based on adjusted wind stress computed with the estimated geostrophic surface currents added to the scatterometer measured winds (see text for details).

between the lag and the curl of the ARC surface currents. The estimated surface currents have an otherwise inconspicuous effect on the magnitude of the scatterometer-measured coupling between surface winds and SST.

8. CLW response to SST perturbations

SST-induced modification of the MABL is also evident in AMSR measurements of CLW. Positive (negative) perturbations in the CLW field are associated with warm (cool) SST perturbations (Fig. 18); the spatial correlation between the 1-yr average SST and CLW perturbations is 0.59. Assuming a cloud liquid water density of 0.1 g m^{-3} for low-level stratocumulus (Rogers and Yau 1996), the typical CLW perturbations of

0.015 mm observed over the ARC correspond to differences of about 300 m between cloud thickness over cold and warm SST perturbations. Although direct measurements of MABL clouds are not available over the ARC, this is of the same order as the stratocumulus thickness of $\sim 300\text{--}400$ m observed by Wang et al. (1999) over the warm water of the midlatitude Azores during the Atlantic Stratocumulus Transition Experiment (ASTEX). Bretherton et al. (2004) observed similar stratocumulus thicknesses over the eastern tropical Pacific Ocean during the East Pacific Investigation of Climate (EPIC) field study during September and October of 2001.

Over the geographic region considered in Fig. 18, the cross correlation between the 1-yr average perturbation SST and CLW is maximum when the perturbation CLW field is lagged 0.5° downwind (eastward) of perturbations in the SST field. This spatial lag, visually evident in Fig. 18, is comparable to spatial lags that have been observed from satellite studies of clouds and SST elsewhere over the ocean. For example, Deser et al. (1993) showed from longitudinal cross sections that anomalies in low-level cloud reflectivity were displaced about 1.25° downwind of warm cusps associated with Pacific tropical instability waves. From in situ measurements along 95°W in the tropical Pacific, Raymond et al. (2004) found that maximum CLW values occur $\sim 1^\circ$ to 2° downwind of the maximum SST gradient associated with the equatorial cold tongue.

It is noteworthy that spatial correlations between the perturbation CLW and wind stress divergence over the ARC were not statistically significant. SST-induced cloud formation is evidently not due to convection from low-level convergence but from MABL deepening due to increased sensible and latent heat fluxes. This is consistent with the results obtained by Wai and Stage (1989) who concluded that the presence of clouds over warmer water is due to the increase in MABL depth through entrainment rather than to a lowering of the lifting condensation level.

9. Conclusions

The Agulhas Return Current is an exceptionally good region to study the MABL modification by spatially varying SST. Satellite microwave measurements of SST that have recently become available from the AMSR have allowed a quantitative reinvestigation of the coupling between wind stress and SST in a previous analysis that was based on the Reynolds SST analyses (O'Neill et al. 2003). The short-scale SST perturbations are much better resolved in the AMSR SST; SST gradients in the ARC region computed from the AMSR

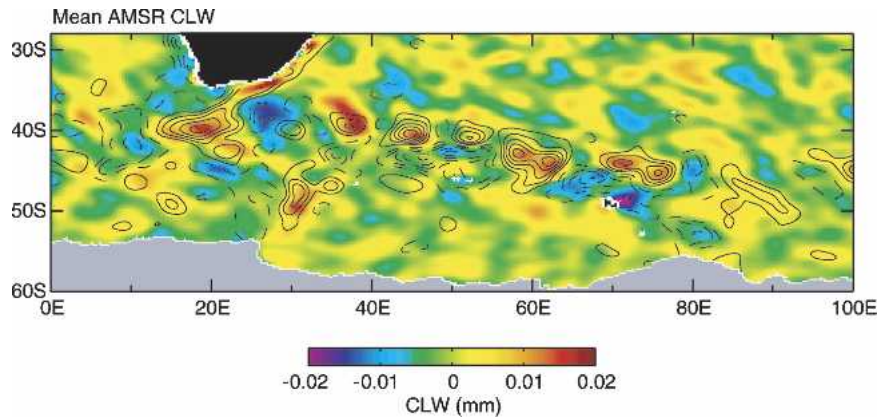


FIG. 18. Map of AMSR measurements of CLW averaged over the 1-yr period 2 Jun 2002 to 7 Jun 2003 and spatially high-pass filtered to attenuate wavelengths longer than 10° latitude by 30° longitude; the contours overlaid are the average perturbation AMSR SST shown in color in the top panel of Fig. 4. The contour interval is 0.5°C and the zero contour has been omitted for clarity.

SST fields are about five times stronger than those computed from the Reynolds SST analyses. SST perturbations induce nearly coincident perturbations in the surface wind stress, sensible heat flux, and cloud liquid water. The responses of the wind stress curl and divergence to SST perturbations are dominated by annual cycles, with responses nearly twice as strong during the wintertime than during the summertime. The analysis of NCEP reanalysis fields in section 6 suggests that this response can be explained by the annual cycle of large-scale lower tropospheric stability. Changes in the observed wind stress perturbations between warm and cool water are too large to be explained by changes in the stability-dependent surface drag coefficient alone.

It should be emphasized that the interaction described here is only part of a complex series of interactions involving the coupled ocean–atmosphere system that includes two-way interactions between the MABL and the upper ocean. The SST-induced wind perturbations cause perturbations in surface heat fluxes and upper-ocean mixing that are likely to erode SST perturbations that will feedback onto the original wind stress perturbations. Moreover, the upwelling associated with SST-induced wind stress curl perturbations will feed back on the ocean, likely altering the SST. These two-way feedbacks are intriguing aspects of the coupled system that can significantly enhance our understanding of coupled ocean–atmosphere interactions.

Acknowledgments. We thank Ricardo Matano, Roger Samelson, Michael Schlax, Deborah Smith, and Rob Wood for helpful discussions during the course of this analysis. We also thank Holda Biskeborn for help in editing this manuscript. We thank two anonymous

reviewers for their thorough reading and helpful comments on our paper that lead to improved discussion of several points in the manuscript. The research presented here was supported by NASA Grants NAS5-32965 and NAG5-12378.

REFERENCES

- Boebel, O., T. Rossby, J. R. E. Lutjeharms, W. Zenk, and C. Barron, 2003: Path and variability of the Agulhas Return Current. *Deep-Sea Res.*, **50**, 35–56.
- Bond, N. A., 1992: Observations of planetary boundary layer structure in the eastern equatorial Pacific. *J. Climate*, **5**, 699–706.
- Bretherton, C. S., and Coauthors, 2004: The EPIC2001 Stratocumulus study. *Bull. Amer. Meteor. Soc.*, **85**, 967–977.
- Chelton, D. B., and M. G. Schlax, 2003: The accuracies of smoothed sea surface height fields constructed from tandem altimeter datasets. *J. Atmos. Oceanic Technol.*, **20**, 1276–1302.
- , F. J. Wentz, C. L. Gentemann, R. A. de Szoeke, and M. G. Schlax, 2000: Satellite microwave SST observations of trans-equatorial tropical instability waves. *Geophys. Res. Lett.*, **27**, 1239–1242.
- , and Coauthors, 2001: Observation of coupling between surface wind stress and sea surface temperature in the eastern tropical Pacific. *J. Climate*, **14**, 1479–1498.
- , M. G. Schlax, M. H. Freilich, and R. F. Milliff, 2004: Satellite measurements reveal persistent small-scale features in ocean winds. *Science*, **303**, doi:10.1126/science.1091901.
- Cleveland, W. S., and S. J. Devlin, 1988: Locally weighted regression: An approach to regression analysis by local fitting. *J. Amer. Stat. Assoc.*, **83**, 596–610.
- Cornillon, P., and K.-A. Park, 2001: Warm core ring velocities inferred from NSCAT. *Geophys. Res. Lett.*, **28**, 575–578.
- Cronin, M. F., S.-P. Xie, and H. Hashizume, 2003: Barometric pressure variations associated with eastern Pacific tropical instability waves. *J. Climate*, **16**, 3050–3057.
- de Szoeke, S. P., and C. S. Bretherton, 2004: Quasi-Lagrangian large eddy simulations of cross-equatorial flow in the east

- Pacific atmospheric boundary layer. *J. Atmos. Sci.*, **61**, 1837–1858.
- Deser, C., J. J. Bates, and S. Wahl, 1993: The influence of sea surface temperature on stratiform cloudiness along the equatorial front in the Pacific Ocean. *J. Climate*, **6**, 1172–1180.
- Freihe, C. A., and Coauthors, 1991: Air–sea fluxes and surface layer turbulence around a sea surface temperature front. *J. Geophys. Res.*, **96**, 8593–8609.
- Hahn, C. J., S. G. Warren, and J. London, 1995: The effect of moonlight on observation of cloud cover at night, and application to cloud climatology. *J. Climate*, **8**, 1429–1446.
- Hashizume, H., S.-P. Xie, W. T. Liu, and K. Takeuchi, 2001: Local and remote atmospheric response to tropical instability waves: A global view from space. *J. Geophys. Res.*, **106**, 10 173–10 185.
- , —, M. Fujiwara, M. Shiotani, T. Watanabe, Y. Tanimoto, W. T. Liu, and K. Takeuchi, 2002: Direct observations of atmospheric boundary layer response to slow SST variations over the eastern equatorial Pacific. *J. Climate*, **15**, 3379–3393.
- Hayes, S. P., M. J. McPhaden, and J. M. Wallace, 1989: The influence of sea surface temperature on surface wind in the eastern equatorial Pacific: Weekly to monthly variability. *J. Climate*, **2**, 1500–1506.
- Hsu, S. A., 1984a: Effect of cold-air advection on internal boundary layer development over warm oceanic currents. *Dyn. Atmos. Oceans*, **8**, 307–319.
- , 1984b: Sea-breeze-like winds across the north wall of the Gulf Stream: An analytical model. *J. Geophys. Res.*, **89**, 2025–2028.
- Jury, M. R., 1994: A thermal front within the marine atmospheric boundary layer over the Agulhas Current south of Africa: Composite aircraft observations. *J. Geophys. Res.*, **99**, 3297–3304.
- , and N. Walker, 1988: Marine boundary layer modification across the edge of the Agulhas Current. *J. Geophys. Res.*, **93**, 647–654.
- Kalnay, E., and Coauthors, 1996: The NCEP/NCAR 40-Year Reanalysis Project. *Bull. Amer. Meteor. Soc.*, **77**, 437–472.
- Kelly, K. A., S. Dickinson, M. J. McPhaden, and G. C. Johnson, 2001: Ocean currents evident in satellite wind data. *Geophys. Res. Lett.*, **28**, 2469–2472.
- Koraćin, D., and D. P. Rogers, 1990: Numerical simulations of the response of the marine atmosphere to ocean forcing. *J. Atmos. Sci.*, **47**, 592–611.
- Kwon, B. H., B. Bénéch, D. Lambert, P. Durand, A. Druilhet, H. Giordani, and S. Planton, 1998: Structure of the marine atmospheric boundary layer over an oceanic thermal front: SEMAPHORE experiment. *J. Geophys. Res.*, **103C**, 25 159–25 180.
- Large, W. G., and S. Pond, 1982: Sensible and latent heat flux measurements over the ocean. *J. Phys. Oceanogr.*, **12**, 464–482.
- Lee-Thorp, A. M., M. Rouault, and J. R. E. Lutjeharms, 1998: Cumulus cloud formation above the Agulhas Current. *S. Afr. J. Sci.*, **94**, 351–354.
- , —, and —, 1999: Moisture uptake in the boundary layer above the Agulhas Current: A case study. *J. Geophys. Res.*, **104**, 1423–1430.
- Levitus, S., and T. P. Boyer, 1994: *Temperature*, Vol. 4, *World Ocean Atlas 1994*, NOAA Atlas NESDIS 4, 117 pp.
- Lindzen, R. S., and S. Nigam, 1987: On the role of sea surface temperature gradients in forcing low-level winds and convergence in the Tropics. *J. Atmos. Sci.*, **44**, 2418–2436.
- Liu, W. T., and W. Tang, 1996: Equivalent neutral wind. JPL Publication 96–17, Pasadena, CA, 8 pp.
- , X. Xie, P. S. Polito, S.-P. Xie, and H. Hashizume, 2000: Atmospheric manifestation of tropical instability waves observed by QuikSCAT and Tropical Rain Measuring Mission. *Geophys. Res. Lett.*, **27**, 2545–2548.
- Lutjeharms, J. R. E., and R. C. van Ballegooyen, 1984: Topographic control in the Agulhas Current system. *Deep-Sea Res.*, **31**, 1321–1337.
- , and I. J. Anson, 2001: The Agulhas Return Current. *J. Mar. Syst.*, **30**, 115–138.
- , R. D. Mev, and I. E. Hunter, 1986: Cloud lines over the Agulhas Current. *S. Afr. J. Sci.*, **82**, 635–640.
- Nonaka, M., and S.-P. Xie, 2003: Covariations of sea surface temperature and wind over the Kuroshio and its extension: Evidence for ocean-to-atmosphere feedback. *J. Climate*, **16**, 1404–1413.
- O’Neill, L. W., D. B. Chelton, and S. K. Esbensen, 2003: Observations of SST-induced perturbations of the wind stress field over the Southern Ocean on seasonal time scales. *J. Climate*, **16**, 2340–2354.
- Peixoto, J. P., and A. H. Oort, 1992: *Physics of Climate*. Springer-Verlag, 520 pp.
- Raymond, D. J., and Coauthors, 2004: EPIC2001 and the coupled ocean–atmosphere system of the tropical east Pacific. *Bull. Amer. Meteor. Soc.*, **85**, 1341–1354.
- Reynolds, R. W., and T. M. Smith, 1994: Improved global sea surface temperature analyses using optimum interpolation. *J. Climate*, **7**, 929–948.
- , N. A. Rayner, T. M. Smith, D. C. Stokes, and W. Wang, 2002: An improved in situ and satellite SST analysis for climate. *J. Climate*, **15**, 1609–1625.
- Rogers, D. P., 1989: The marine boundary layer in the vicinity of an ocean front. *J. Atmos. Sci.*, **46**, 2044–2062.
- Rogers, R. R., and M. K. Yau, 1996: *A Short Course in Cloud Physics*. Butterworth-Heinemann, 290 pp.
- Rossov, W. B., and R. A. Schiffer, 1991: ISCCP cloud data products. *Bull. Amer. Meteor. Soc.*, **72**, 2–20.
- Rouault, M., and A. M. Lee-Thorp, 1996: Fine-time resolution measurements of atmospheric boundary layer properties between Cape Town and Marion Island. *S. Afr. J. Mar. Sci.*, **17**, 281–296.
- , and J. R. E. Lutjeharms, 2000: Air–sea exchange over an Agulhas eddy at the subtropical convergence. *Global Atmos. Ocean Syst.*, **7**, 125–150.
- Schlag, M. G., D. B. Chelton, and M. H. Freilich, 2001: Sampling errors in wind fields constructed from single and tandem scatterometer datasets. *J. Atmos. Oceanic Technol.*, **18**, 1014–1036.
- Small, J. R., S.-P. Xie, and Y. Wang, 2003: Numerical simulation of atmospheric response to Pacific tropical instability waves. *J. Climate*, **16**, 3723–3741.
- , —, —, S. K. Esbensen, and D. Vickers, 2005: Numerical simulation of boundary layer structure and cross-equatorial flow in the eastern Pacific. *J. Atmos. Sci.*, **62**, 1812–1830.
- Stull, R. B., 1988: *An Introduction to Boundary Layer Meteorology*. Kluwer Academic, 666 pp.
- Sweet, W. R., R. Fett, J. Kerling, and P. LaViolette, 1981: Air–sea interaction effects in the lower troposphere across the north wall of the Gulf Stream. *Mon. Wea. Rev.*, **109**, 1042–1052.
- Thum, N., S. K. Esbensen, D. B. Chelton, and M. J. McPhaden, 2002: Air–sea heat exchange along the northern sea surface

- temperature front in the eastern tropical Pacific. *J. Climate*, **15**, 3361–3378.
- Trenberth, K. E., W. G. Large, and J. G. Olson, 1990: The mean annual cycle in global ocean wind stress. *J. Phys. Oceanogr.*, **20**, 1742–1760.
- Wai, W. M., and S. A. Stage, 1989: Dynamical analysis of marine atmospheric boundary layer structure near the Gulf Stream oceanic front. *Quart. J. Roy. Meteor. Soc.*, **115**, 29–44.
- Wallace, J. M., T. P. Mitchell, and C. Deser, 1989: The influence of sea surface temperature on surface wind in the eastern equatorial Pacific: Seasonal and interannual variability. *J. Climate*, **2**, 1492–1499.
- Wang, J., W. B. Rossow, T. Uttal, and M. Rozendaal, 1999: Variability of cloud vertical structure during ASTEX observed from a combination of rawinsonde, radar, ceilometer, and satellite. *Mon. Wea. Rev.*, **127**, 2484–2502.
- Warner, T. T., M. N. Lakhtakia, J. D. Doyle, and R. A. Pearson, 1990: Marine atmospheric boundary layer circulations forced by Gulf Stream sea surface temperature gradients. *Mon. Wea. Rev.*, **118**, 309–323.
- Wentz, F. J., and T. Meissner, 2000: Algorithm theoretical basis document, Version 2, AMSR Ocean Algorithm. [Available online at: www.remss.com/papers/AMSR_Ocean_Algorithm_Version_2.doc.]
- , C. L. Gentemann, D. Smith, and D. B. Chelton, 2000: Satellite measurements of sea surface temperature through clouds. *Science*, **288**, 847–850.
- White, W. B., and J. L. Annis, 2003: Coupling of extratropical mesoscale eddies in the ocean to westerly winds in the atmospheric boundary layer. *J. Phys. Oceanogr.*, **33**, 1095–1107.
- Xie, S.-P., M. Ishiwatari, H. Hashizume, and K. Takeuchi, 1998: Coupled ocean–atmosphere waves on the equatorial front. *Geophys. Res. Lett.*, **25**, 3863–3866.
- , W. T. Liu, Q. Liu, and M. Nonaka, 2001: Far-reaching effects of the Hawaiian Islands on the Pacific ocean–atmosphere system. *Science*, **292**, 2057–2060.